THE JOURNAL OF PHYSICAL CHEMISTRY Letters

Letter

pubs.acs.org/JPCL

Lead-Free Halide Double Perovskites via Heterovalent Substitution of Noble Metals

George Volonakis,[†] Marina R. Filip,[†] Amir Abbas Haghighirad,[‡] Nobuya Sakai,[‡] Bernard Wenger,[‡] Henry J. Snaith,*[,‡] and Feliciano Giustino*[,†]

[†]Department of Materials, University of Oxford, Parks Road, Oxford OX1 3PH, United Kingdom

[‡]Department of Physics, Clarendon Laboratory, University of Oxford, Parks Road, Oxford OX1 3PU, United Kingdom

Supporting Information

ABSTRACT: Lead-based halide perovskites are emerging as the most promising class of materials for next-generation optoelectronics; however, despite the enormous success of lead-halide perovskite solar cells, the issues of stability and toxicity are yet to be resolved. Here we report on the computational design and the experimental synthesis of a new family of Pb-free inorganic halide double perovskites based on bismuth or antimony and noble metals. Using first-principles calculations we show that this hitherto unknown family of perovskites exhibits very promising optoelectronic properties, such as tunable band gaps in the visible range and low carrier effective masses. Furthermore, we successfully synthesize the double perovskite $Cs_2BiAgCl_6$, perform structural refinement using single-crystal X-ray diffraction, and characterize its optical properties via optical absorption and photoluminescence measurements. This new perovskite belongs to the $Fm\bar{3}m$ space group and consists of $BiCl_6$ and $AgCl_6$ octahedra alternating in a rock-salt face-centered cubic structure. From UV−vis and photoluminescence measurements we obtain an indirect gap of 2.2 eV.

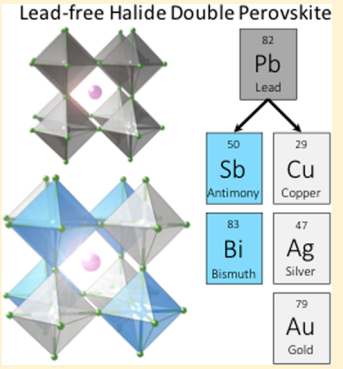

Perovskites are among the most fascinating crystals and play important roles in a variety of applications, including ferroelectricity, piezoelectricity, high-T_c superconductivity, ferromagnetism, giant magnetoresistance, photocatalysis, and photovoltaics.[1−8] The majority of perovskites are oxides and are very stable under ambient temperature and pressure conditions;[4,9] however, this stability is usually accompanied by very large band gaps; therefore, most oxide perovskites are not suitable candidates for optoelectronic applications. The most noteworthy exceptions are the ferroelectric perovskite oxides related to $LiNbO_3$, $BaTiO_3$, $Pb(Zr, Ti)O_3$, and $BiFeO_3$, which are being actively investigated for photovoltaic applications, reaching power conversion efficiencies of up to 8%.[9] The past 5 years witnessed a revolution in optoelectronic research with the discovery of the organic−inorganic lead-halide perovskite family. These solution-processable perovskites are fast, becoming the most promising materials for the next generation of solar cells, achieving efficiencies above 20%.[10−13] Despite this breakthrough, hybrid lead-halide perovskites are known to degrade due to moisture and heat,[14] upon prolonged exposure to light,[15] and are prone to ion or halide vacancy migration, leading to unstable operation of photovoltaic devices.[16,17] At the same time the presence of lead raises concerns about the potential environmental impact of these materials.[18,19] Given these limitations, identifying a stable, nontoxic halide perovskite optoelectronic material is one of the key challenges to be addressed in the area of perovskite optoelectronics.

The starting point of our search for a lead-free halide-perovskite is the prototypical inorganic compound $CsPbI_3$. $CsPbI_3$ is an ABX_3 perovskite where the heavy metal cations Pb^{2+} and the halide anions I^- occupy the B and X sites, respectively, while Cs^+ occupies the A site. The most obvious route to replacing Pb in this compound is via substitution of other group-14 elements, such as Sn and Ge; however, both elements tend to undergo oxidation, for example, from Sn^{2+} to Sn^{4+}, leading to a rapid degradation of the corresponding halide perovskites.[20−23] More generally, it should also be possible to substitute lead by other divalent cations outside of group-14 elements; however, our previous high-throughput computational screening of potential candidates showed that the homovalent substitution of lead in halide perovskites negatively impacts the optoelectronic properties by increasing band gaps and effective masses.[24]

Another possible avenue is to consider heterovalent substitution, that is, the formation of a double perovskite structure with a basic formula unit $A_2B'B''X_6$.[4] This type of compound is abundant in the case of oxides and is well-known for its ferroelectric, ferromagnetic, and multiferroic properties.[4] Additionally, double perovskites have been explored to tune the band gap of oxide perovskites.[25,26] On the contrary, halide double perovskites remain a much less explored class of materials. To date, the best known halide double perovskites are based on alkali and rare-earth metals and are investigated for applications as scintillators in radiation detectors.[27]

The B′ and B″ sites have to be occupied by one monovalent and one trivalent cation to replace the divalent Pb cations and

Received: February 18, 2016
Accepted: March 16, 2016

DOI: 10.1021/acs.jpclett.6b00376
J. Phys. Chem. Lett. XXXX, XXX, XXX−XXX

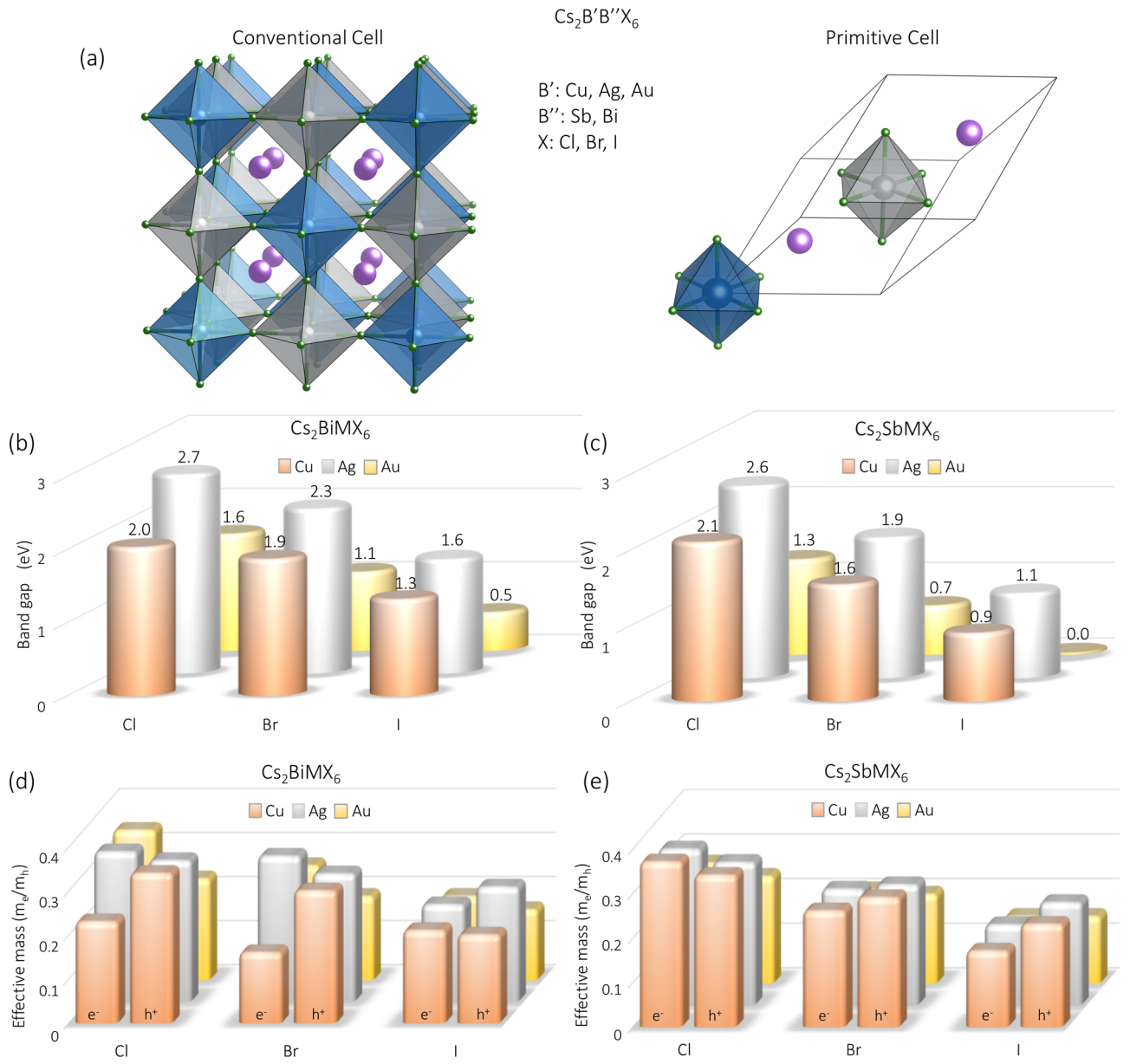

Figure 1. Computational screening of the electronic properties of the pnictogen noble-metal halide double perovskites. (a) Polyhedral model of the conventional (left) and reduced (right) unit cell of the hypothetical halide double perovskites. The pnictogen (B′) and noble-metal (B″) cations alternate along the three crystallographic axes, forming the rock-salt ordering. (b) Electronic band gaps calculated for all compounds in the halide double perovskite family using the PBE0 hybrid functionals. All calculated band gaps are indirect with the top of the valence band at the *X* point $(0,0,2\pi/a)$ of the Brillouin zone, where *a* is the lattice parameter of the FCC unit cell. The bottom of the conduction band is at the *L* point $(\pi/a, \pi/a, \pi/a)$ of the Brillouin zone in all cases, except $Cs_2BiAgCl_6$, $Cs_2BiCuCl_6$, and $Cs_2BiCuBr_6$, where the bottom of the conduction band is found at the Γ (0,0,0) point. (c) Conductivity effective masses calculated from DFT/LDA for each compound (see the Supporting Information). The effective masses are calculated at the VBM (holes) and CBM (electrons) in each case.

maintain the total charge neutrality. We search for our B'^{3+} metallic cations among the pnictogens and consider Bi and Sb as the most suitable choices. Arsenic is less desirable owing to its toxicity. For the monovalent cations we choose the noble metals Cu, Ag, and Au. From elementary considerations Cu, Ag, and Au appear very promising for optoelectronic applications. In fact, in their metallic form, the noble metals are the best known electrical conductors, owing to their filled d^{10} shell and the free-electron-like behavior of the s^1 shell. In addition, in an octahedral environment, the ionic radii of Cu^+ (0.91 Å), Ag^+ (1.29 Å), and Au^+ (1.51 Å) are similar to those of Pb^{2+} (1.19 Å), Sb^{3+} (0.76 Å), and Bi^{3+} (1.03 Å).[28] We note that the cost of the precursors for the proposed Pb alternatives (AgCl and CuCl) is similar to the case of lead, except for the case of gold (AuCl), which is considerably more expensive. Following this simple reasoning we investigate hypothetical halide double perovskites with the pairs B′/B″, where B′ = Sb, Bi and B″ = Cu, Ag, Au.

We investigate the electronic properties of these hypothetical compounds from first-principles using density functional theory (DFT) in the local density approximation (LDA). We construct "rock-salt" double perovskites, whereby B′ and B″ alternate in every direction (shown in Figure 1a). The rock-salt ordering is known to be the ground state for most oxide double

DOI: 10.1021/acs.jpclett.6b00376
J. Phys. Chem. Lett. XXXX, XXX, XXX−XXX

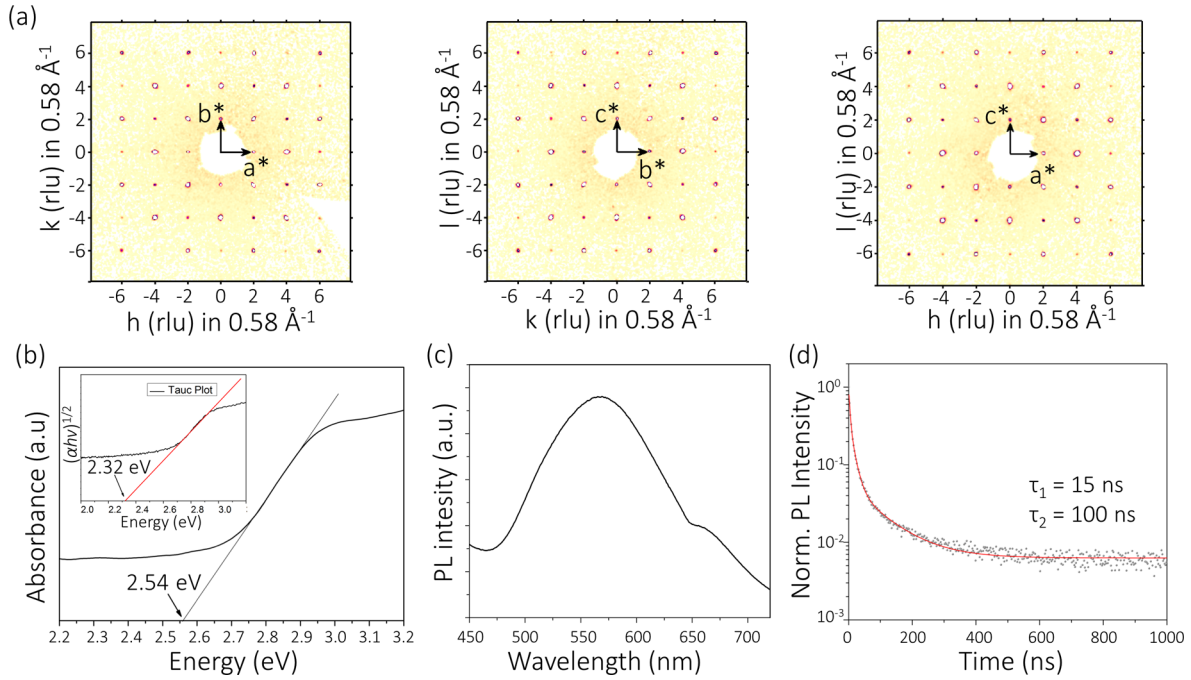

Figure 2. Experimental synthesis and characterization of $Cs_2BiAgCl_6$. (a) X-ray diffraction pattern for a $Cs_2BiAgCl_6$ single crystal at 293 K. *hkl* shown for three different planes, that is, 0*k*l, *h*0*l*, and *hk*0. All wave vectors are labeled in reciprocal lattice units (rlu), and a*, b*, and c* denote reciprocal lattice vectors of the cubic cell of the $Fm\bar{3}m$ structure. (b) UV−vis optical absorption spectrum of $Cs_2BiAgCl_6$. The inset shows the Tauc plot, corresponding to an indirect allowed transition (assuming the expression: $(\alpha h\nu)^{1/2} = C(h\nu - E_g)$, where α is the absorption coefficient, $h\nu$ is the energy of the incoming photon, E_g is the optical band gap, and C is a constant). The straight lines are fitted to the linear regions of the absorption spectrum and Tauc plot, and the intercepts at 2.32 and 2.54 eV marked on the plot are calculated from the fit. (c) Steady-state photoluminescence (PL) spectrum of $Cs_2BiAgCl_6$, deposited on glass. (d) Time-resolved photoluminescence decay of $Cs_2BiAgCl_6$, deposited on glass. The data are fitted using a biexponential decay function. The decay lifetimes of 15 (fast) and 100 ns (slow) are estimated from the fit.

perovskites;[4] therefore it can be expected to hold also in the present case. For each model structure we perform full structural optimization using DFT-LDA and calculate the electronic band gaps using the hybrid PBE0 functional, as described in the Supporting Information.

In Figure 1b,c we show a comparative view of the band gaps calculated for the entire $Cs_2B'B''X_6$ family. We find that all band gaps are below 2.7 eV, spanning the visible and near-infrared optical spectrum. The band gaps are indirect and increase as we move up the halogen or the pnictogen column in the periodic table but do not follow a monotonic trend with respect to the size of the noble-metal cation. This behavior can be explained by the character of the electronic states at the band edges. Indeed, as shown in Figure S1 of the Supporting Information, the conduction band bottom and valence band top in each case are predominantly of pnictogen-p and halogen-p character, respectively. As we move up in the periodic table the energy of the halogen-p states decreases, thus lowering the energy of the valence band top. Similarly, the energy of the pnictogen-p states decreases when moving up in the periodic table, thus lowering the energy of the conduction band bottom. The electron and hole effective masses calculated at the band edges exhibit an anisotropic behavior in most cases (see Table S1). Throughout the entire family of compounds the electron masses are more isotropic than the hole masses. For clarity, in Figure 1 we report the conductivity effective masses,[29] as defined in the Supporting Information. We note that all compounds exhibit small carrier effective masses between 0.1 and 0.4 m_e, very close to those calculated for $CH_3NH_3PbI_3$ within the same level of theory.[30]

The electronic band structures of these halide double perovskites (shown in Figures S2 and S3) exhibit several features of particular interest. In all cases, the valence band maximum (VBM) is at the X $(0,0,2\pi/a)$ point in the Brillouin zone. The conduction band minimum (CBM) is at Γ (0,0,0) for $Cs_2BiAgCl_6$, $Cs_2BiCuCl_6$, and $Cs_2BiCuBr_6$, while for the other compounds the CBM is at the L $(\pi/a, \pi/a, \pi/a)$ point. In Figure S4, we show the band structure of $Cs_2BiAgCl_6$ calculated in the conventional unit cell (which corresponds to four primitive cells and contains eight octahedra in a cubic lattice). Here, as a result of Brillouin zone folding, the band gap of $Cs_2BiAgCl_6$ becomes direct at the Γ point, although the direct transition is still forbidden by symmetry. This suggests an avenue for engineering a direct band gap in these compounds. In fact, symmetry can be broken by inducing octahedral tilts, and this could be achieved by varying the steric size of the A-site cation (Cs).[31] For example, this effect could be realized by incorporating an organic cation, like methylammonium or formamidinium into the cuboctahedral cavity. To demonstrate this point, we report in Figure S5 the calculated band structure of the hypothetical orthorhombic compound $MA_2BiAgCl_6$ (MA = CH_3NH_3, methylammonium; the structure is constructed as described in the Supporting Information). Explicit calculations of the optical matrix elements indicate that the direct optical transition in the methylammonium-based compound is allowed, as expected.

Having established that the family of $A_2B'B''X_3$ halide double perovskites, based on B′ = Sb, Bi and B″ = Cu, Ag, Au, exhibits promising optoelectronic properties, we move to the synthesis and optical characterization of a representative member of this group of compounds. We adapt the synthesis process of

DOI: 10.1021/acs.jpclett.6b00376
J. Phys. Chem. Lett. XXXX, XXX, XXX−XXX

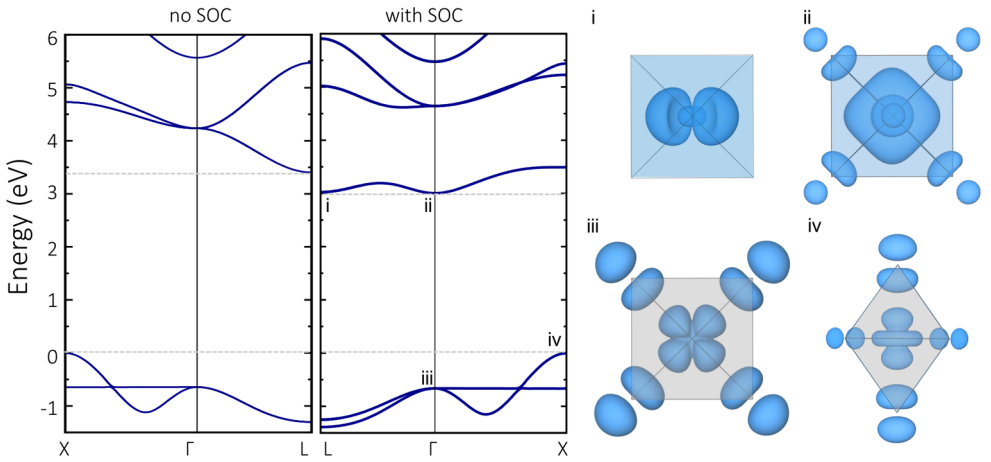

Figure 3. Electronic structure properties calculated for the experimental crystal structure of $Cs_2BiAgCl_6$. Band structure of $Cs_2BiAgCl_6$ calculated along the high-symmetry path $L(\pi/a, \pi/a, \pi/a) - \Gamma(0,0,0) - X(0,0,2\pi/a)$ without (left) and with (right) spin−orbit coupling. The black points on the fully relativistic band structure marked "i−iv" mark the conduction band bottom at L and Γ and the valence band top at Γ and X, respectively. For each of the states we show the electronic wave functions. The conduction band bottom is primarily of Bi-p and Cl-p character, while the valence band top consists of Ag-d and Cl-p character. The shape of all four wave functions is consistent with metal-halide σ bonds.

$Cs_2BiNaCl_6$, reported in ref 32 to allow for the incorporation of a noble metal. Of the three noble metals under consideration, Ag has an ionic radius that is closest to that of Na (1.02 vs 1.15 Å). For this reason we proceed to synthesize $Cs_2BiAgCl_6$ by conventional solid-state reaction, as described in detail in the Supporting Information. In Figure 2a we show the X-ray diffraction pattern for a single crystal (~30 μm diameter). We observe sharp reflections for the crystallographic 0*kl*, *h*0*l*, and *hk*0 planes. These reflections show characteristics of $m\bar{3}m$ symmetry that reveal systematic absences for (hkl; $h + k$, $k + l$, $h + l = 2n$) corresponding to the face-centered space groups $F432$, $F\bar{4}3m$, and $Fm\bar{3}m$. The latter was selected for structure refinement after confirmation that $Cs_2BiAgCl_6$ crystallizes in an FCC lattice. We find that there is no significant distortion of octahedral symmetry about the Bi^{3+}. The atomic positions from the structural refinement are listed in Table S2 of the Supporting Information. The X-ray diffraction patterns uniquely identify the $Fm\bar{3}m$ (no. 225) space group at room temperature, and the quantitative structural analysis gives a very good description of the data. In addition, our crystal structure refinement is consistent with the rock-salt configuration assumed by our atomistic model. The experimental and computationally predicted conventional lattice parameters are in very good agreement, 10.78 and 10.50 Å, respectively. From the optical absorption spectrum and Tauc plot (see Figure 2b), we can estimate an indirect optical band gap in the range of 2.3 to 2.5 eV. The indirect character of the band gap is consistent with the broad photoluminescence peak observed between 480 and 650 nm (1.9 to 2.6 eV) with the maximum at ~575 nm (2.2 eV), red-shifted with respect to the optical absorption onset. In addition, the time-resolved photoluminescence decay shown in Figure 2c was fitted with a double exponential giving a fast component lifetime of 15 ns and a slow component lifetime of 100 ns. The as-made compound appears to be stable under ambient conditions for weeks after synthesis, with the bright-yellow color persisting and no visible changes appearing in the powder X-ray diffraction patterns (see Figures S6 and S7).

In Figure 3 we show the electronic band structure of $Cs_2BiAgCl_6$ calculated for the as-determined experimental crystal structure, with and without relativistic spin−orbit coupling effects. The features of the valence band edge are almost unchanged when the relativistic effects are included. This is consistent with the predominant Cl-p and Ag-d character of this band. By contrast, because of the large spin−orbit coupling, the conduction band edge splits in two bands, separated by >1.5 eV at the Γ point. This effect is not surprising given that the character of the conduction band bottom is of primarily Bi-p character. For comparison, in the case of $Cs_2SbAgCl_6$ (see Figure S8) the spin−orbit splitting of the conduction band at the Γ point is of only 0.5 eV. The fundamental band gap is reduced by 0.4 eV upon inclusion of relativistic effects, and the shape of the conduction band is drastically different. Therefore, the inclusion of spin−orbit coupling is crucial for the correct description of the conduction band edge, bearing resemblance to the case of $CH_3NH_3PbI_3$.[33,34] In the fully relativistic case we calculated an indirect band gap of 3.0 eV and lowest direct transition of 3.5 eV, in very close agreement with the results obtained for the model $Cs_2BiAgCl_6$ structure, discussed in Figure 1 (2.7 eV (indirect) and 3.3 eV (direct)). The small difference in band gap of 0.2 to 0.3 eV is due to the small difference in volume between the experimental and predicted crystal structure. The calculated electronic band gaps are overestimated with respect to the measured optical band gap by ~0.5 eV. This quantitative discrepancy does not affect the qualitative physical trends of the band gaps discussed throughout this work and can be associated with the approximations employed in our PBE0 calculations. A better agreement with experiment can be reached by fine-tuning the fraction of exact exchange or by performing GW calculations.[35,36] The latter will be reported in a future work.

In summary, through a combined theoretical and experimental study, we have designed a new family of halide double-perovskite semiconductors based on pnictogens and noble metals. We used state-of-the-art first-principles calculations to explore trends in the electronic and optical properties in the entire family of double perovskites $A_2B'B''X_6$ with A = Cs; B′ = Bi, Sb; B″ = Cu, Ag, Au; and X = Cl, Br, I. Our calculations revealed highly tunable carrier effective masses and optical gaps across the visible range of the electromagnetic spectrum. We predicted all compounds to be indirect gap semiconductors and

DOI: 10.1021/acs.jpclett.6b00376
J. Phys. Chem. Lett. XXXX, XXX, XXX−XXX

proposed a simple strategy for turning them into direct-gap materials. We successfully synthesized $Cs_2BiAgCl_6$ and obtained a face-centered cubic double perovskite. Optical characterization confirmed our theoretical predictions, indicating an indirect gap semiconductor. Overall, the present work is the first detailed description of the structure and optoelectronic properties of the pnictogen noble-metal halide double perovskite family and calls for many future experimental and theoretical studies to assess the full potential of these new materials. We expect that a complete mapping of the genome of halide double perovskites based on pnictogens and noble metals may unlock a world of new functional materials for photovoltaics, photocatalysis, photodetectors, light-emitting devices, piezoelectrics, and magnetoelectrics.

■ ASSOCIATED CONTENT

Supporting Information

The Supporting Information is available free of charge on the ACS Publications website at DOI: 10.1021/acs.jpclett.6b00376.

Description of the computational setup and details of the materials synthesis and characterization and crystallographic data. All electronic band structures for the pnictogen noble-metal double-halide perovskites. Additional Figures relevant to the discussions in this article. (PDF)

■ AUTHOR INFORMATION

Corresponding Authors

*E-mail: feliciano.giustino@materials.ox.ac.uk. Phone: (+44) 1865 612790

*E-mail: henry.snaith@physics.ox.ac.uk. Phone: (+44) 01865 272380.

Author Contributions

G.V. and M.R.F. contributed equally to this work.

Notes

The authors declare no competing financial interest.

■ ACKNOWLEDGMENTS

The research leading to these results has received funding from the Graphene Flagship (EU FP7 grant no. 604391), the Leverhulme Trust (Grant RL-2012-001), the U.K. Engineering and Physical Sciences Research Council (Grant No. EP/J009857/1 and EP/M020517/1), and the European Union Seventh Framework Programme (FP7/2007-2013) under grant agreement nos. 239578 (ALIGN) and 604032 (MESO). we acknowledge the use of the University of Oxford Advanced Research Computing (ARC) facility (http://dx.doi.org/10.5281/zenodo.22558) and the ARCHER UK National Supercomputing Service under the "AMSEC" Leadership project. G.V., M.R.F., and F.G. thank Marios Zacharias for useful discussions. Figures involving atomic structures were rendered using VESTA.[37]

■ REFERENCES

(1) Suntivich, J.; Gasteiger, H. A.; Yabuuchi, N.; Nakanishi, H.; Goodenough, J. B.; Shao-Horn, Y. *Nat. Chem.* **2011**, *3*, 546−550.

(2) Stranks, S.; Snaith, H. J. *Nat. Nanotechnol.* **2015**, *10*, 391.

(3) Grätzel, M. *Nat. Mater.* **2014**, *13*, 838.

(4) Vasala, S.; Karppinen, M. *Prog. Solid State Chem.* **2015**, *43*, 1−36.

(5) Grinberg, L.; West, D. V.; Torres, M.; Gou, G.; Stein, D. M.; Wu, L.; Chen, G.; Gallo, E. M.; Akbashev, A. R.; Davies, P. K.; Spanier, J. E.; Rappe, A. M. *Nature* **2013**, *503*, 509−512.

(6) Ramesh, R.; Spaldin, N. A. *Nat. Mater.* **2007**, *6*, 21−29.

(7) Rijnders, G.; Blank, D. H. A. *Nature* **2005**, *433*, 369−370.

(8) Ahn, C. H.; Rabe, K. M.; Triscone, J.-M. *Science* **2004**, *303*, 488−491.

(9) Fan, Z.; Sun, K.; Wang, J. *J. Mater. Chem. A* **2015**, *3*, 18809.

(10) Green, M.; Ho-Baillie, A.; Snaith, H. J. *Nat. Photonics* **2014**, *8*, 506.

(11) Lee, M. M.; Teuscher, J.; Miyasaka, T.; Murakami, T. N.; Snaith, H. J. *Science* **2012**, *338*, 643.

(12) Kim, H.-S.; Lee, C. R.; Im, J.-H.; Lee, K.-B.; Moehl, T.; Marchioro, A.; Moon, S.-J.; Humphry-Baker, R.; Yum, J.-H.; Moser, J. E.; Grätzel, M.; Park, N.-G. *Sci. Rep.* **2012**, *2*, 591.

(13) Best Research-Cell Efficiencies. http://www.nrel.gov/ncpv/.

(14) Manser, J. S.; Saidaminov, M. I.; Christians, J. A.; Bakr, O. M.; Kamat, P. V. *Acc. Chem. Res.* **2016**, *49*, 330−338.

(15) Hoke, E. T.; Slotcavage, D. J.; Dohner, E. R.; Bowring, A. R.; Karunadasa, H. I.; McGehee, M. D. *Chem. Sci.* **2015**, *6*, 613−617.

(16) Eames, C.; Frost, J. M.; Barnes, P. R. F.; O'Regan, B. C.; Walsh, A.; Saiful Islam, M. *Nat. Commun.* **2015**, *6*, 7497.

(17) Meloni, S.; Moehl, T.; Tress, W.; Franckevicius, M.; Saliba, M.; Lee, Y. H.; Gao, P.; Nazeeruddin, M. K.; Zakeeruddin, S. M.; Rothlisberger, U.; Grätzel, M. *Nat. Commun.* **2016**, *7*, 10334.

(18) Espinosa, N.; Serrano-Luján, L.; Urbina, A.; Krebs, F. C. *Sol. Energy Mater. Sol. Cells* **2015**, *137*, 303.

(19) Babayigit, A.; Thanh, D. D.; Ethirajan, A.; Manca, J.; Muller, M.; Boyen, H.-G.; Conings, B. *Sci. Rep.* **2016**, *6*, 18721.

(20) Stoumpos, C. C.; Malliakas, C. D.; Kanatzidis, M. G. *Inorg. Chem.* **2013**, *52*, 9019.

(21) Baikie, T.; Fang, Y.; Kadro, J. M.; Schreyer, M.; Wei, F.; Mhaisalkar, S. G.; Grätzel, M.; White, T. J. *J. Mater. Chem. A* **2013**, *1*, 5628.

(22) Hao, F.; Stoumpos, C. C.; Cao, D. H.; Chang, R. P. H.; Kanatzidis, M. G. *Nat. Photonics* **2014**, *8*, 489.

(23) Noel, N.; Stranks, S. D.; Abate, A.; Wehrenfennig, C.; Guarnera, S.; Haghighirad, A.-A.; Sadhanala, A.; Eperon, G. E.; Pathak, S. K.; Johnston, M. B.; Petrozza, A.; Herz, L. M.; Snaith, H. J. *Energy Environ. Sci.* **2014**, *7*, 3061.

(24) Filip, M. R.; Giustino, F. *J. Phys. Chem. C* **2016**, *120*, 166−173.

(25) Nechache, R. N.; Harnagea, C.; Li, S.; Cardenas, L.; Huang, W.; Chakrabartty, J.; Rosei, F. *Nat. Photonics* **2014**, *9*, 61−67.

(26) Berger, R. F.; Neaton, J. B. *Phys. Rev. B: Condens. Matter Mater. Phys.* **2012**, *86*, 165211.

(27) van Loef, E. V. D.; Dorenbos, P.; van Eijk, C. W. E.; Krämer, K. W.; Güdel, H. U. *J. Phys.: Condens. Matter* **2002**, *14*, 8481−8496.

(28) Shannon, R. D. *Acta Crystallogr., Sect. A: Cryst. Phys., Diffr., Theor. Gen. Crystallogr.* **1976**, *32*, 751−767.

(29) He, Y.; Galli, G. *Chem. Mater.* **2014**, *26*, 5394.

(30) Filip, M. R.; Verdi, C.; Giustino, F. *J. Phys. Chem. C* **2015**, *119*, 25209−25219.

(31) Filip, M. R.; Eperon, G.; Snaith, H. J.; Giustino, F. *Nat. Commun.* **2014**, *5*, 5757.

(32) Morrs, L. R.; Robinson, W. R. *Acta Crystallogr., Sect. B: Struct. Crystallogr. Cryst. Chem.* **1972**, *28*, 653−654.

(33) Even, J.; Pedesseau, L.; Jancu, J.-M.; Katan, C. *J. Phys. Chem. Lett.* **2013**, *4*, 2999.

(34) Filip, M. R.; Giustino, F. *Phys. Rev. B: Condens. Matter Mater. Phys.* **2014**, *90*, 245145.

(35) Hedin, L. *Phys. Rev.* **1965**, *139*, A796.

(36) Hybertsen, M. S.; Louie, S. G. *Phys. Rev. B: Condens. Matter Mater. Phys.* **1986**, *34*, 5390.

(37) Momma, K.; Izumi, F. *J. Appl. Crystallogr.* **2008**, *41*, 653.

(38) Slavney, A. H.; Hu, T.; Lindenberg, A. M.; Karunadasa, H. I. *J. Am. Chem. Soc.* **2016**, *138*, 2138−2141.

(39) McClure, E. T.; Ball, M. R.; Windl, W.; Woodward, P. M. *Chem. Mater.* **2016**, *28*, 1348−1354.

■ NOTE ADDED IN PROOF

During the preparation of this manuscript we became aware of the publication of two related papers: ref 38 (published

DOI: 10.1021/acs.jpclett.6b00376
J. Phys. Chem. Lett. XXXX, XXX, XXX−XXX

February 7, 2016) and ref 39 (published February 10th, 2016). The key difference between the present work and that of refs 38 and 39 is that we perform a computational screening of the entire family of pnictogen noble-metal double-halide perovskites and perform experiments that confirm our predictions.

DOI: 10.1021/acs.jpclett.6b00376
J. Phys. Chem. Lett. XXXX, XXX, XXX−XXX

Supporting Information for: Lead-Free Halide Double Perovskites via Heterovalent Substitution of Noble Metals

George Volonakis,[†,¶] Marina R. Filip,[†,¶] Amir Abbas Haghighirad,[‡] Nobuya Sakai,[‡] Bernard Wenger,[‡] Henry J. Snaith,[*,‡] and Feliciano Giustino[*,†]

†*Department of Materials, University of Oxford, Parks Road OX1 3PH, Oxford, UK*

‡*Department of Physics, University of Oxford, Clarendon Laboratory, Parks Road, Oxford OX1 3PU, UK*

¶*These authors contributed equally to this work*

E-mail: feliciano.giustino@materials.ox.ac.uk; henry.snaith@physics.ox.ac.uk

Phone: (+44) 1865 612790 ; (+44) 01865 272380

Computational setup

Structural optimizations. Structural optimizations are performed using DFT/LDA calculations,[1,2] planewaves, and pseudopotentials, as implemented in the `Quantum ESPRESSO` distribution.[3] For Cl, Br, I, Cu, Ag, Au, Bi and Sb we use fully relativistic ultrasoft pseudopotentials[4,5] including nonlinear core correction,[6] while for C, N, H we use non-relativistic ultrasoft pseudopotentials. For Cs we use a norm-conserving pseudopotential[7] All other pseudopotentials are from the `Quantum ESPRESSO` or Theos library (`http://theossrv1.epfl.ch/Main/Pseudopotentials`). The planewaves kinetic energy cutoffs for the wavefunctions and charge density are set to 60 Ry and 300 Ry. The Brillouin zone is sampled using an unshifted 10×10×10 grid. Forces and total energies are converged to 10 meV/Å and 1 meV, respectively. All calculations are carried out using fully-relativistic LDA including spin-orbit coupling. The structures corresponding to the inorganic double perovskites are fully optimized starting from a face-centered cubic unit cell, belonging to the $Fm\bar{3}m$ symmetry space group, as reported for the double perovskite $Cs_2BiNaCl_6$.[8] Each unit cell comprises of 10 atoms (two octahedra, one centered at the pnictogen atom, the other centered at the noble metal). The hypothetical hybrid organic-inorganic structure of $(CH_3NH_3)_2BiAgCl_6$ is optimized starting from the orthorhombic Pnma structure of $CH_3NH_3PbI_3$ reported in Ref.,[9] maintaining the alternating 'rock-salt' structure. This unit cell contains 48 atoms (four octahedra, two centered at the pnictogen atom and two centered at the noble metal).

Band gap calculations. In order to overcome the underestimated electronic band gaps calculated within DFT-LDA, we employ hybrid functional calculations using the PBE0 method.[10,11] Although approximate, this choice is expected to be reliable for assessing band gap trends. The PBE0 calculations are carried out including spin-orbit coupling effects, using `VASP`,[12] the projector-augmented wave method,[13] and a kinetic energy cutoff of 300 eV. A Γ-centered 4×4×4 k-point grid was used to sample the Brillouin zone. Using a 5×5×5 k-point grid the electronic band gap at Γ changes by less than 0.01 eV for $Cs_2BiAgCl_6$.

Band structure calculations. All band structures are calculated within LDA including

spin-orbit coupling. In all band structures shown in the manuscript, the conduction bands are rigidly shifted by a scissor correction to match the fundamental band gap as calculated from PBE0.

Effective masses. All carrier effective masses are calculated within fully-relativistic LDA, using a finite-differences formula with increments of $5 \cdot 10^{-3}\big(2\pi/a\big)$, where a is the lattice parameter of the unit cell. The anisotropy ratio of the effective mass tensor M is defined as $\mathrm{norm}\big[M - \mathrm{trace}(M)I/3\big]/\mathrm{norm}(M)$, where I is the identity matrix (this ratio can be between 0 and 100%). The conductivity effective masses reported in Figure 1 are calculated by performing the harmonic average over the three eigenvalues of the effective mass tensor in each case.

Materials synthesis and characterization

Synthesis. Single-phase samples of $Cs_2BiAgCl_6$ were prepared by conventional solid-state reaction in a sealed fused silica ampoule. For a typical reaction, the starting materials CsCl (Sigma Aldrich, 99.9%), $BiCl_3$ (Sigma Aldrich, 99.99%) and AgCl (Sigma Aldrich, 99%) were mixed in a molar ratio 2:1:1, respectively. The mixture was loaded in a fused silica ampoule that was flame sealed under vacuum (10^{-3} Torr). The mixture was heated to 500°C over 5 hours and held at 500°C for 4 hours. After cooling to room temperature, a yellow polycrystalline material was formed. Octahedral shaped crystals of length ∼0.1 mm could be extracted from the powder sample that later were used to determine the crystal structure.

Film fabrication. $Cs_2BiAgCl_6$ powder was dispersed in poly methyl methacrylate (PMMA) in Toluene. To form films, the dispersion was spin-coated on a glass slide at 1500 rpm. This was repeated several times to attain uniform thick film.

Structural characterization. Powder X-ray diffraction was carried out using a Panalytical X'pert powder diffractometer (Cu-Kα1 radiation; λ = 154.05 pm) at room temperature. Structural parameters were obtained by Rietveld refinement using General Structural Analysis Software.[14,15] Single crystal data were collected for $Cs_2BiAgCl_6$ at room temperature using an Agilent Supernova diffractometer that uses Mo Kα beam with λ = 71.073 pm and

is fitted with an Atlas detector. Data integration and cell refinement was performed using CrysAlis Pro Software by Agilent Technogies Ltd, Yarnton, Oxfordshire, England. The structure was analysed by Patterson and Direct methods and refined using SHELXL 2014 software package.[16]

Film characterization. A Varian Cary 300 UV-Vis spectrophotometer with an integrating sphere was used to acquire absorbance spectra and to account for reflection and scattering. Time-resolved photo-luminescence measurements were acquired using a time correlated single photon counting (TCSPC) setup (FluoTime 300, PicoQuant GmbH). Film samples were photoexcited using a 397 nm laser head (LDH_P-C-405, PicoQuant GmbH) pulsed at frequencies of 200 kHz. The steady-state photoluminescence (PL) measurements were taken using an automated spectrofluorometer (Fluorolog, Horiba Jobin-Yvon), with a 450 W-Xenon lamp excitation.

Table S1: Diagonal elements of the hole and electron effective mass tensors calculated from DFT-LDA, and the anisotropy ratio calculated in each case as described in the Computational Setup. All values are reported in units of the electron mass.

	holes				electrons			
	m_1	m_2	m_3	$\alpha(\%)$	m_1	m_2	m_3	$\alpha(\%)$
$Cs_2SbCuCl_6$	0.71	0.71	0.17	51	0.48	0.33	0.33	21
$Cs_2SbCuBr_6$	0.64	0.64	0.14	52	0.34	0.24	0.24	20
Cs_2SbCuI_6	0.52	0.52	0.11	53	0.23	0.15	0.15	22
$Cs_2SbAgCl_6$	0.70	0.70	0.16	52	0.42	0.33	0.33	14
$Cs_2SbAgBr_6$	0.63	0.63	0.13	53	0.31	0.24	0.24	14
Cs_2SbAgI_6	0.52	0.52	0.11	53	0.22	0.16	0.16	17
$Cs_2SbAuCl_6$	0.67	0.67	0.11	56	0.30	0.30	0.24	13
$Cs_2SbAuBr_6$	0.56	0.56	0.09	56	0.22	0.22	0.20	8
Cs_2SbAuI_6	0.42	0.42	0.07	56	0.15	0.15	0.15	2
$Cs_2BiCuCl_6$	0.66	0.66	0.17	49	0.23	0.23	0.23	0
$Cs_2BiCuBr_6$	0.58	0.58	0.15	49	0.16	0.16	0.16	0
Cs_2BiCuI_6	0.48	0.48	0.13	48	0.34	0.18	0.18	32
$Cs_2BiAgCl_6$	0.63	0.63	0.16	49	0.34	0.34	0.34	0
$Cs_2BiAgBr_6$	0.57	0.57	0.15	50	0.48	0.28	0.28	27
Cs_2BiAgI_6	0.49	0.49	0.13	48	0.33	0.19	0.19	28
$Cs_2BiAuCl_6$	0.50	0.50	0.11	52	0.37	0.33	0.33	8
$Cs_2BiAuBr_6$	0.41	0.41	0.09	52	0.30	0.25	0.25	12
Cs_2BiAuI_6	0.32	0.32	0.08	50	0.25	0.17	0.17	20

Table S2: Crystallographic data for a $Cs_2BiAgCl_6$ single crystal.

Compound	$Cs_2BiAgCl_6$
Measurement temperature	293 K
Crystal system	Cubic
Space group	$Fm\bar{3}m$
Unit cell dimensions	a = 10.777 ± 0.005 Å
	$\alpha = \beta = \gamma = 90°$
Volume	1251.68 Å^3
Z	4
Density (calculated)	4.221 g/cm^3
Reflections collected	3434
Unique reflections	82 from which 0 suppressed
R(int)	0.1109
R (sigma)	0.0266
Goodness-of-fit	1.151
Final R indices (R_{all})	0.0212
wR_{obs}	0.0322
Wavelength	0.71073 Å

Weight scheme for the refinement	Weight = 1/[sigma^2(Fo^2)+(0.0074 * P)^2+0.00*P] where P = (Max(Fo^2,0)+2*Fc^2)/3

Isotropic temperature factors (Å^2)	U_{iso} (Cs) 0.04284 ± 0.00044, (Bi) 0.02103 ± 0.00040 , (Ag) 0.02384 ± 0.00048, (Cl) 0.05063 ± 0.00107

Anisotropic temperature factor (Å^2)	U_{11}(Cs) = 0.04284 ± 0.00044, U_{11}(Bi) = 0.02103 ± 0.00040, U_{11}(Ag) = 0.02384 ± 0.00048, U_{11}(Cl) = 0.02039 ± 0.00149, U_{22}(Cs) = 0.04248 ± 0.00044, U_{22}(Bi) = 0.02103 ± 0.00040, U_{22}(Ag) = 0.02384 ± 0.00048, U_{22}(Cl) = 0.06567 ± 0.00152, U_{33}(Cs) = 0.04248 ± 0.00044, U_{33}(Bi) = 0.02103 ± 0.00040, U_{33}(Ag) = 0.02384 ± 0.00048, U_{33}(Cl) = 0.06567 ± 0.00152

Atomic Wyckoff-positions	Atom	Site	x	y	z	site occupancy
	Cs	8c	0.25	0.25	0.25	1
	Bi	4a	0	0	0	1
	Ag	4b	0.5	0.5	0.5	1
	Cl	24e	0.2489	0	0	1

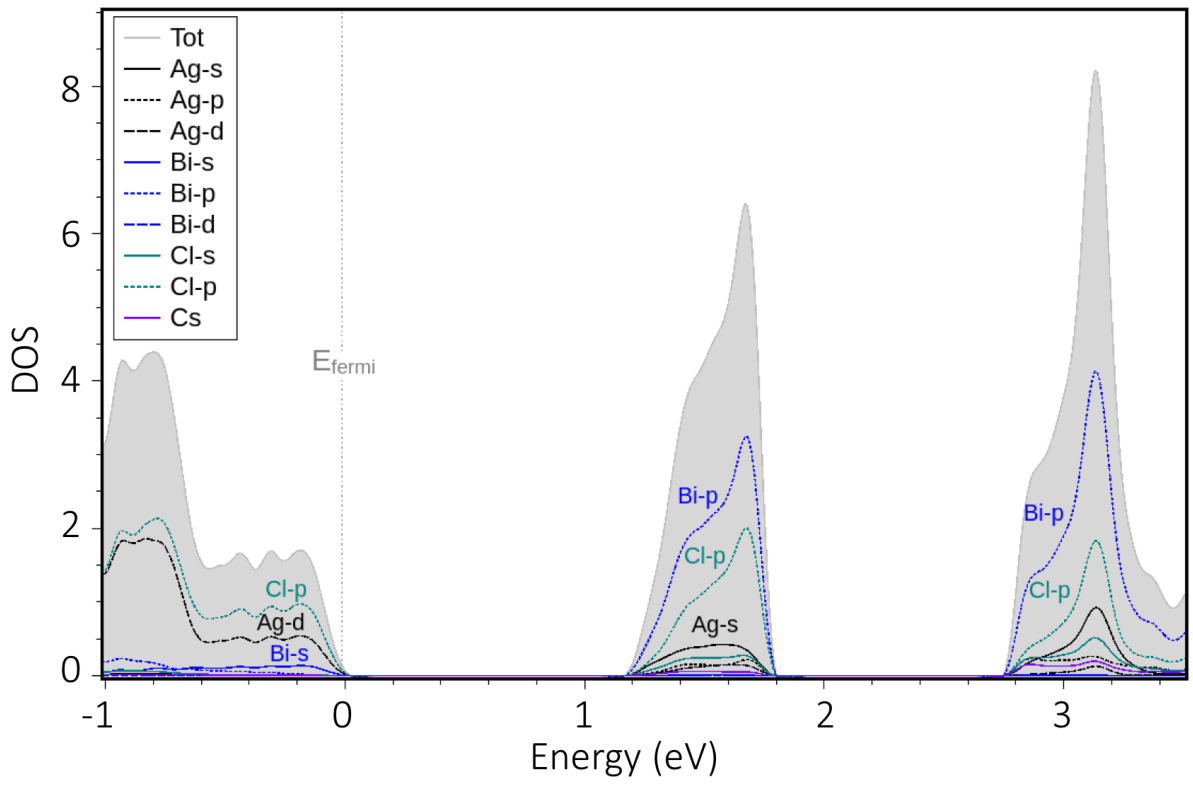

Figure S1: Projected density of states within the DFT-LDA of $Cs_2BiAgCl6$ experimental crystal structure shown in Figure 3. The valence band top is of Cl-*p*, Ag-*d* and Bi-*s* character. The bottom of the conduction band is of Bi-*p*, Cl-*p* and Ag-*s* character. The energy is referred to the top of the valence band.

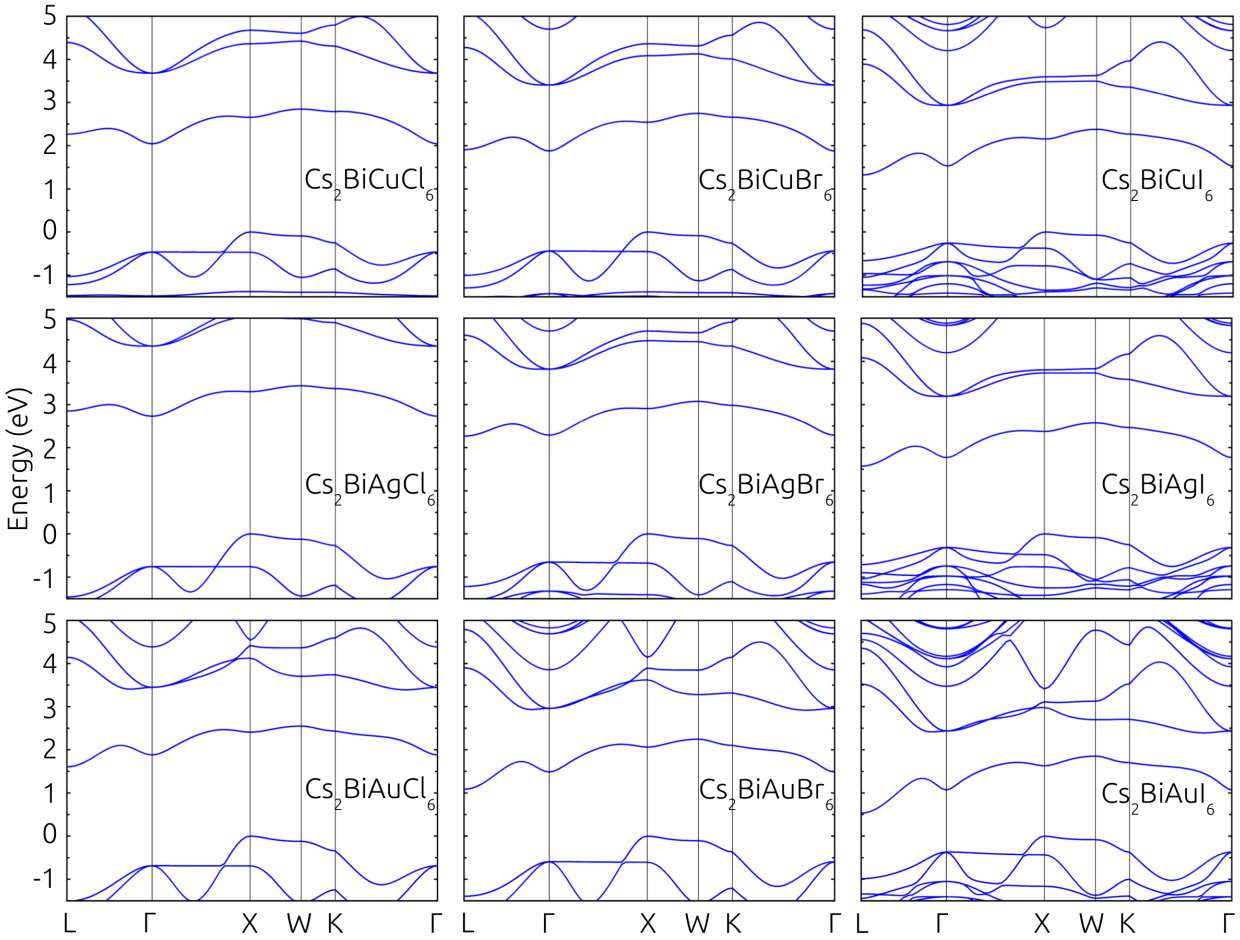

Figure S2: Electronic band structure of all bismuth-based halide double perovskites calculated from DFT-LDA including spin-orbit coupling. For all band structures the conduction band is blue-shifted so that the band gap corresponds to the PBE0 gap, as reported in Figure 1.

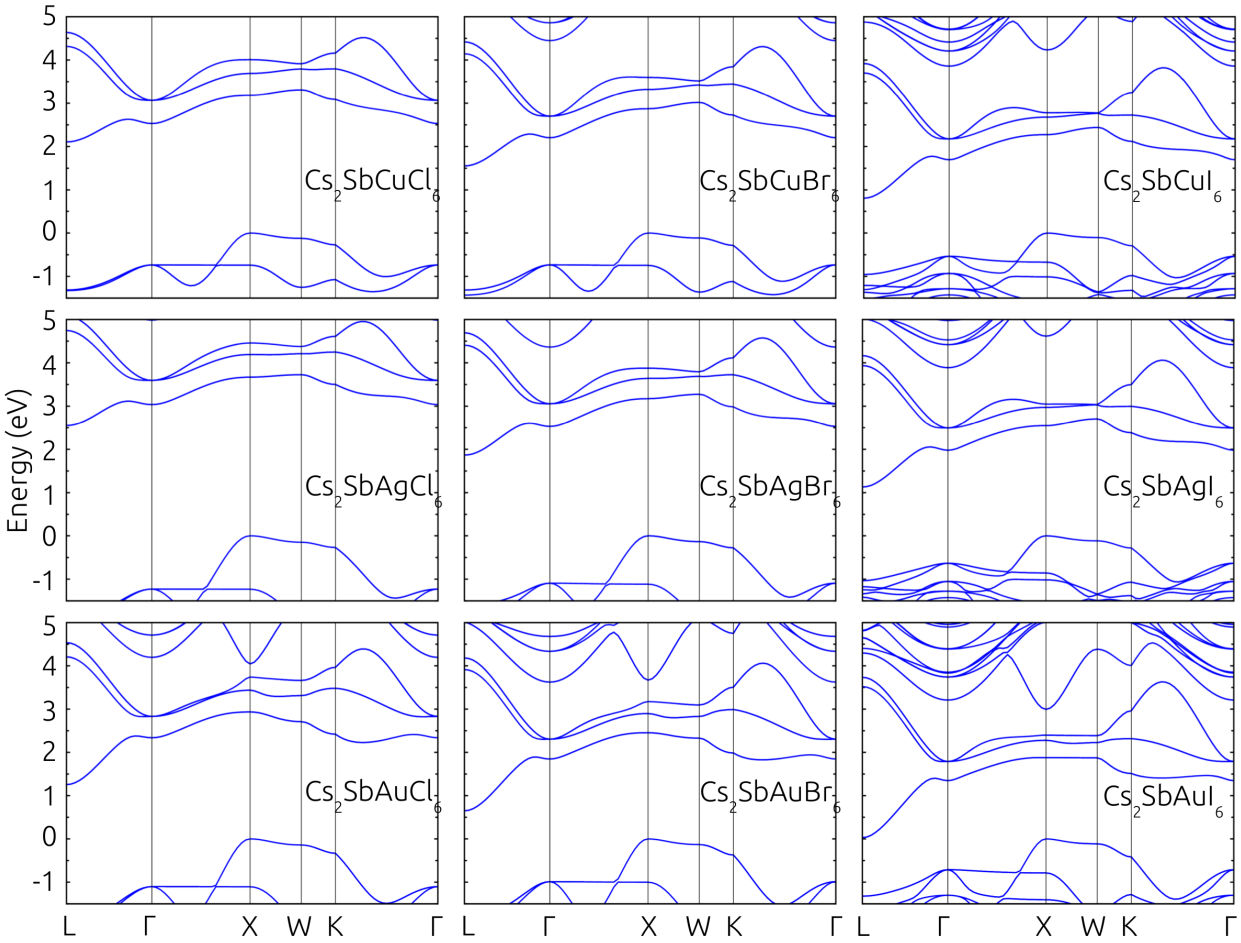

Figure S3: Electronic band structure of all antimony-based halide double perovskites calculated from DFT-LDA including spin-orbit coupling. For all band structures the conduction band is blue-shifted so that the band gap corresponds to the PBE0 gap, as reported in Figure 1.

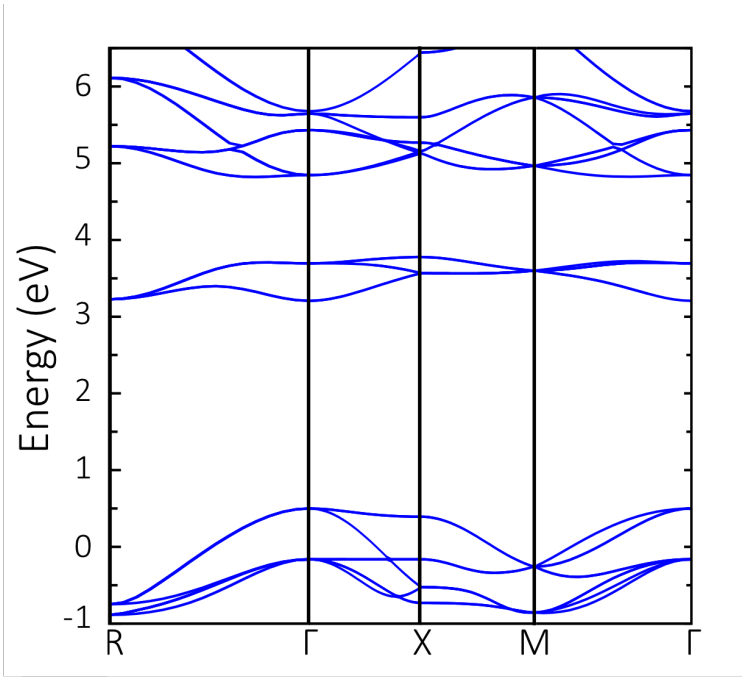

Figure S4: Electronic band structures of $Cs_2BiAgCl6$ double perovskite employing the conventional unit-cell. The band folding along the Γ-X direction moves the top of the valence band from X (shown in Figure S2) to Γ (the conduction band is blue-shifted so that the band gap corresponds to the PBE0 gap).

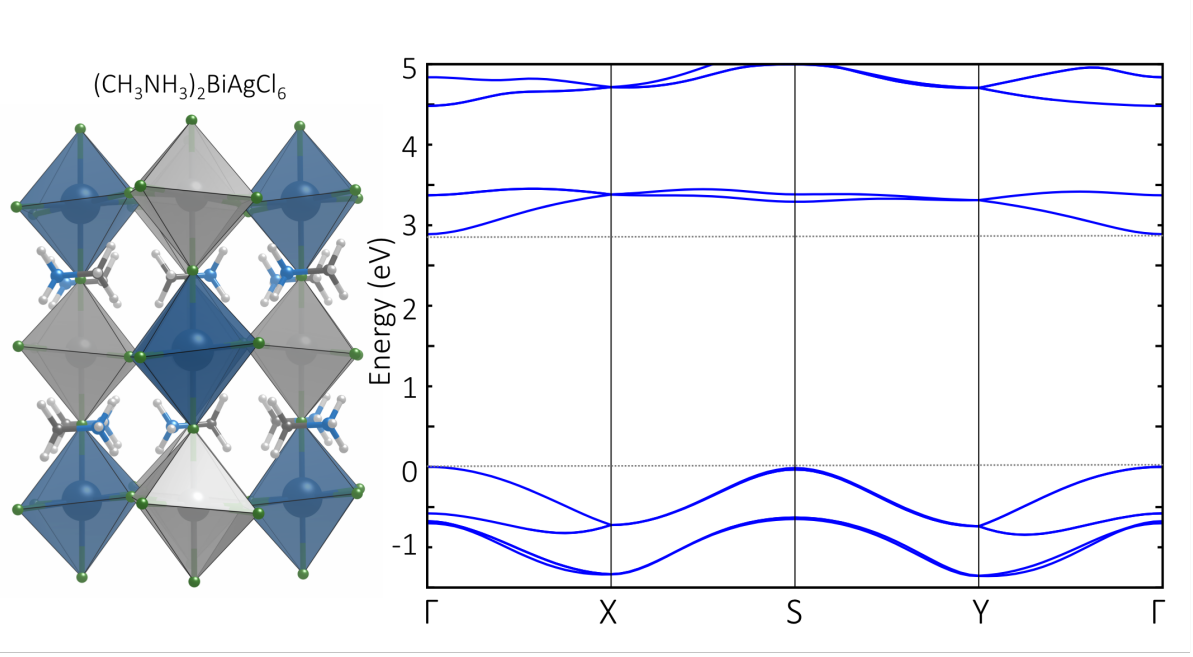

Figure S5: Optimized DFT-LDA crystal structure of the hypothetical $(CH_3NH_3)_2BiAgCl_6$ double perovskite, and corresponding electronic band structure. The crystal structure is orthorhombic and is constructed from the Pnma structure of $CH_3NH_3PbI_3$, as described in the Computational methods. The top of the valence and the bottom of the conduction band are at Γ (the conduction band is blue-shifted so that the band gap corresponds to the PBE0 gap).

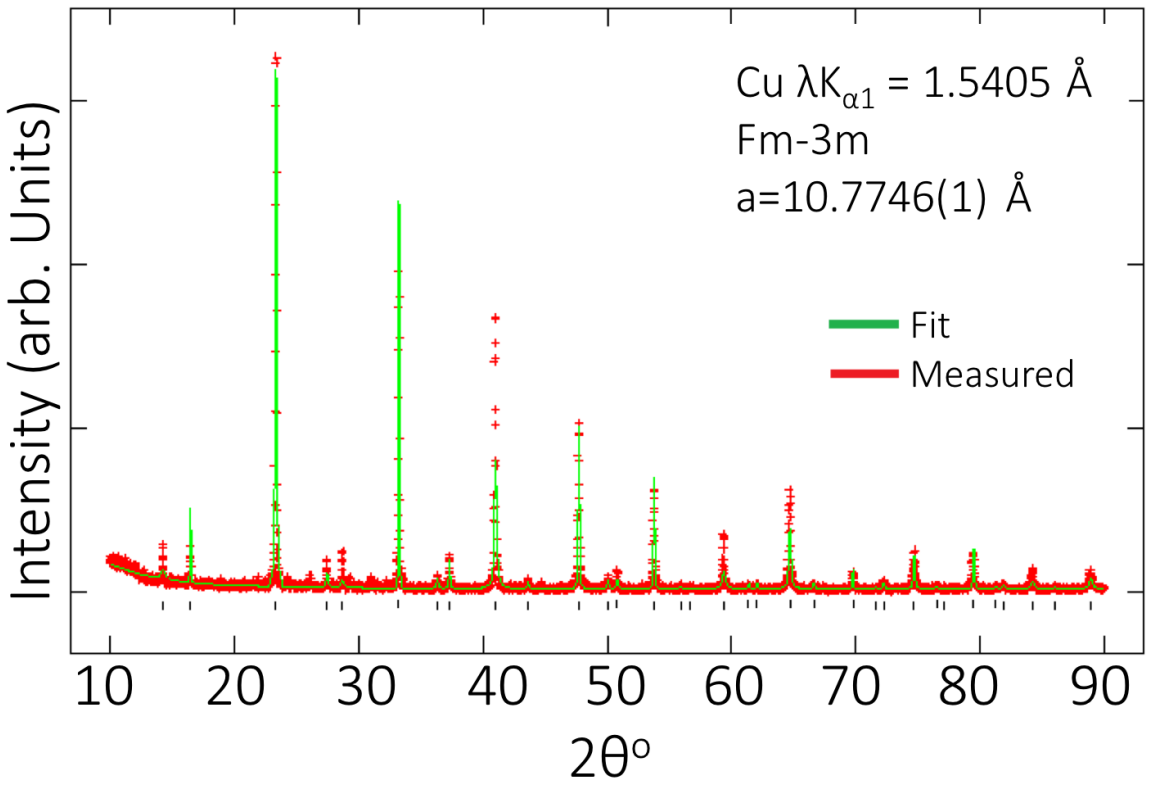

Figure S6: Powder X-ray Diffraction for $Cs_2BiAgCl_6$ data measured at room temperature (red crosses) and fit (green line). The lattice parameter, a of the conventional unit cell is marked on the plot and is in very good agreement with the single-crystal data shown in Table S2.

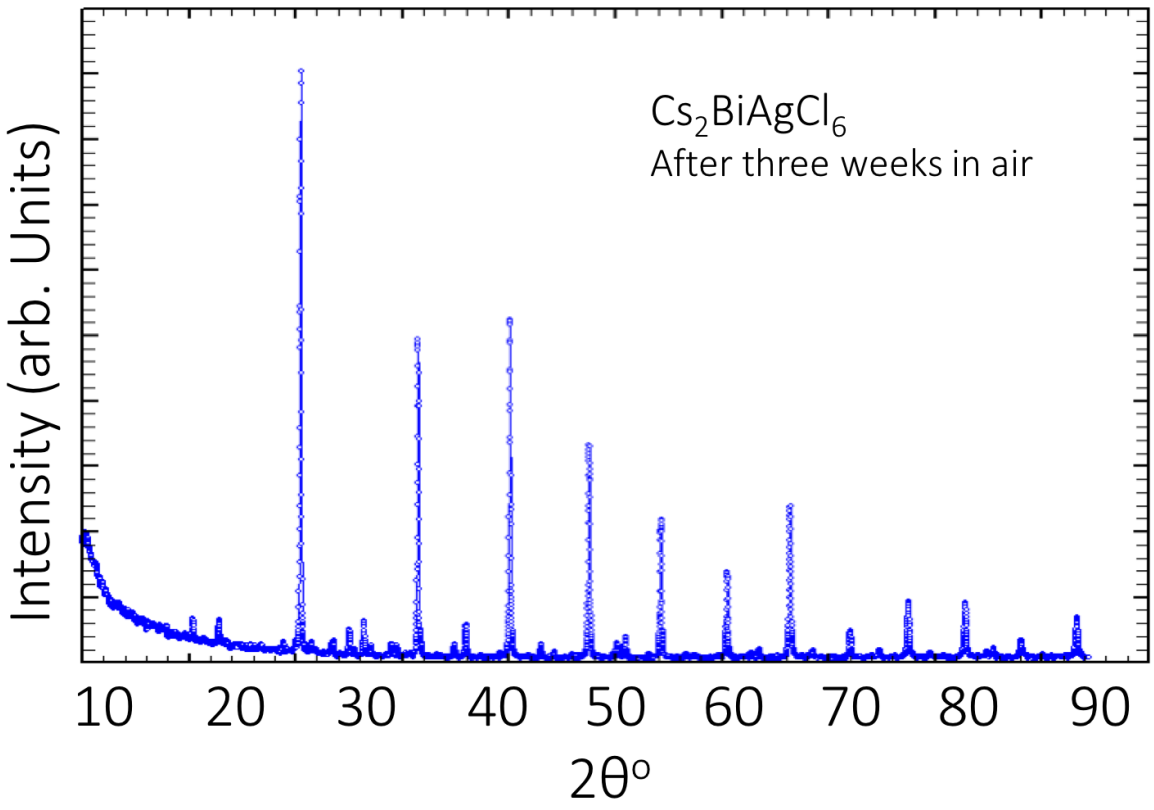

Figure S7: Powder X-ray Diffraction for $Cs_2BiAgCl_6$ data measured at room temperature after three weeks of exposure to ambient conditions.

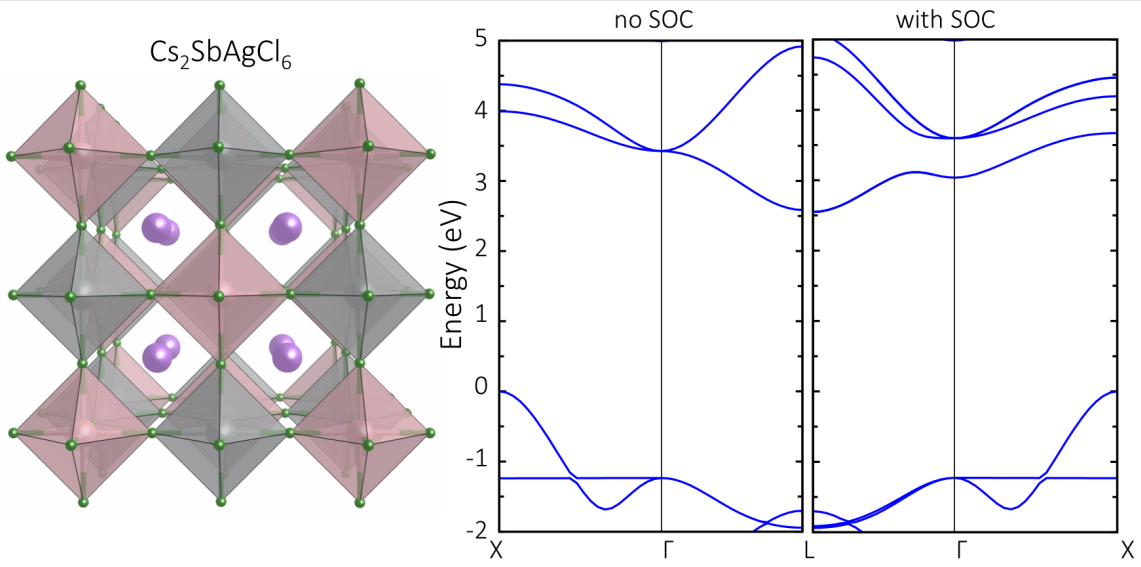

Figure S8: Optimized DFT-LDA crystal structure of $Cs_2SbAgCl_6$ double perovskite and corresponding electronic band structure without (left) and with (right) spin orbit coupling (the conduction bands are blue-shifted so that the band gap corresponds to the PBE0, gap reported in Figure 1).

References

(1) Perdew, J. P.; Zunger, A. Self-Interaction Correction to Density-Functional Approximations for Many-Electrons Systems. *Phys. Rev. B* **1981**, *23*, 5048.

(2) Hohenberg, P.; Kohn, W. Inhomogeneous Electron Gas. *Phys. Rev.* **1964**, *136*, B864.

(3) Giannozzi, P.; Baroni, S.; Bonini, N.; Calandra, M.; Car, R.; Cavazzoni, C.; Ceresoli, D.; Chiarotti, G.; Cococcioni, M.; Dabo, I. et al. QUANTUM ESPRESSO: a modular and open-source software project for quantum simulations of materials. *J. Phys.: Condens. Matter.* **2009**, *21*.

(4) Vanderbilt, D. Soft Self-Consistent Pseudopotentials in a Generalized Eigenvalue Formalism. *Phys. Rev. B* **1990**, *41*, 7892.

(5) Rappe, A. M.; Rabe, K. M.; Kaxiras, E.; Joannopoulos, J. D. Optimized Pseudopotentials. *Phys. Rev. B* **1990**, *41*, 1227.

(6) Louie, S. G.; Froyen, S.; Cohen, M. L. Nonlinear Ionic Pseudopotentials in Spin-Density-Functional Calculations. *Phys. Rev. B* **1982**, *26*, 1738.

(7) Troullier, N.; Martins, J. L. Efficient Pseudopotentials for Plane-Wave Calculations. *Phys. Rev. B* **1991**, *43*, 1993.

(8) Morrs, L. R.; Robinson, W. R. Crystal Structure of $Cs_2BiNaCl_6$. *Acta Cryst. B* **1972**, *28*, 653–654.

(9) Baikie, T.; Fang, Y.; Kadro, J. M.; Schreyer, M.; Wei, F.; Mhaisalkar, S. G.; Grätzel, M.; White, T. J. Synthesis and Crystal Chemistry of the Hybrid Perovskite ($CH_3NH_3PbI_3$) for Solid-State Sensitized Solar Applications. *J. Chem. Mater. A* **2013**, *1*, 5628.

(10) Perdew, B. K., J. P.; Ernzerhof, M. Generalized Gradient Approximation Made Simple. *Phys. Rev. Lett.* **1996**, *77*, 3865.

(11) Paier, H. R. M. M. K. G., J. The Perdew-Burke-Ernzerhof Exchange-Correlation Functional Applied to the G2-1 Test Set Using a Plane-Wave Basis Set. *J. Chem. Phys.* **2005**, *122*, 234102.

(12) Kresse, G.; Furthmuller, J. Efficient Iterative Schemes For *ab initio* Total-Energy Calculations Using a Plane-Wave Basis Set. *Phys. Rev. B* **1996**, *54*, 11169–11186.

(13) Blöchl, P. E. Projector Augmented-Wave Method. *Phys. Rev. B* **1994**, *50*, 17953–17979.

(14) Larson, A. C.; Von Drele, R. B. General Structure Analysis System (GSAS). *Los Alamos National Laboratory Report LAUR* **2000**, 86–748.

(15) Toby, B. H. EXPGUI, A Graphical User Interface for GSAS. *J. Appl. Cryst.* **2001**, *34*, 210–234.

(16) Sheldrick, G. M. Crystal Structure Refinement with SHELXL. *Acta Cryst. C* **2015**, *71-1*, 3.